A principled approach to conductivity uncertainty analysis in electric field calculations

Guilherme B. Saturnino [a,b], Axel Thielscher [a,b], Kristoffer H. Madsen [a,c], Thomas R. Knösche [d,f], Konstantin Weise [d,e,*]

[a] *Danish Research Centre for Magnetic Resonance, Centre for Functional and Diagnostic Imaging and Research, Copenhagen University Hospital Hvidovre, Kettegard Allé 30, DK-2650, Hvidovre, Denmark*
[b] *Technical University of Denmark, Department of Electrical Engineering, Kongens Lyngby, Ørsteds Plads, DK-2800, Kgs. Lyngby, Denmark*
[c] *Technical University of Denmark, Department of Applied Mathematics and Computer Science, Richard Petersens Plads, DK-2800, Kgs. Lyngby, Denmark*
[d] *Max Planck Institute for Human Cognitive and Brain Sciences, Stephanstr. 1a, DE-04103, Leipzig, Germany*
[e] *Technische Universität Ilmenau, Advanced Electromagnetics Group, Helmholtzplatz 2, DE-98693, Ilmenau, Germany*
[f] *Technische Universität Ilmenau, Institute of Biomedical Engineering and Informatics, Gustav-Kirchhoff Str. 2, DE-98693, Ilmenau, Germany*

ARTICLE INFO

ABSTRACT

Uncertainty surrounding ohmic tissue conductivity impedes accurate calculation of the electric fields generated by non-invasive brain stimulation. We present an efficient and generic technique for uncertainty and sensitivity analyses, which quantifies the reliability of field estimates and identifies the most influential parameters. For this purpose, we employ a non-intrusive generalized polynomial chaos expansion to compactly approximate the multidimensional dependency of the field on the conductivities. We demonstrate that the proposed pipeline yields detailed insight into the uncertainty of field estimates for transcranial magnetic stimulation (TMS) and transcranial direct current stimulation (tDCS), identifies the most relevant tissue conductivities, and highlights characteristic differences between stimulation methods. Specifically, we test the influence of conductivity variations on (i) the magnitude of the electric field generated at each gray matter location, (ii) its normal component relative to the cortical sheet, (iii) its overall magnitude (indexed by the 98th percentile), and (iv) its overall spatial distribution. We show that TMS fields are generally less affected by conductivity variations than tDCS fields. For both TMS and tDCS, conductivity uncertainty causes much higher uncertainty in the magnitude as compared to the direction and overall spatial distribution of the electric field. Whereas the TMS fields were predominantly influenced by gray and white matter conductivity, the tDCS fields were additionally dependent on skull and scalp conductivities. Comprehensive uncertainty analyses of complex systems achieved by the proposed technique are not possible with classical methods, such as Monte Carlo sampling, without extreme computational effort. In addition, our method has the advantages of directly yielding interpretable and intuitive output metrics and of being easily adaptable to new problems.

1. Introduction

Transcranial magnetic stimulation (TMS) and transcranial direct current stimulation (tDCS) are two popular non-invasive neuro-stimulation techniques. For an accurate prediction of the neural effect of such stimulation, we need to accurately estimate the electric field induced in the brain. To achieve this, numerical techniques such as the finite element method (FEM) are required due to the complex structure of the brain (Windhoff et al., 2013; Opitz et al., 2015). These techniques rely on knowledge of the electrical conductivities of the head tissues to be incorporated in the simulations. However, reliable measurements of these conductivities are difficult to obtain and the results vary considerably between experimental conditions, subjects, and even repetitions of the same experiment (Geddes and Baker, 1967; Gabriel et al., 1996). A recent in-vivo validation study by Huang et al. (Huang et al., 2017; Huang et al., 2018) showed that conductivity optimization yields values that are comparable to standard values reported in the literature, e.g. for skull ~0.02 S/m, for scalp ~0.2 S/m, and for white matter ~0.38 S/m (Huang et al., 2018). However, the optimal values varied considerably between subjects. For these reasons, one needs to systematically analyze

---

* Corresponding author. Max Planck Institute for Human Cognitive and Brain Sciences, Stephanstr. 1a, 04103, Leipzig, Germany.
  E-mail address: kweise@cbs.mpg.de (K. Weise).

ARTICLE IN PRESS

G.B. Saturnino et al.   NeuroImage xxx (xxxx) xxx

how the uncertainty in tissue conductivity translates into an uncertainty of the predicted electric field. As we have many tissues with uncertain conductivity in the head, we are challenged by having to analyze a transfer function in a large multidimensional space. Therefore, doing this in the classical way, such as using a naive Monte Carlo approach would require producing many samples of the computationally expensive FEM models. Here, we describe a principled approach for uncertainty quantification based on a non-intrusive generalized polynomial chaos (gPC) expansion (Wiener, (1938); Ghanem et al. 2016) to bypass the aforementioned difficulties. We quantify the uncertainty of the electric field caused by the given uncertainties of the tissue conductivities, based on an accurate and effective polynomial surrogate of the transfer function (or functional dependence) between conductivities and fields (Weise et al., 2015; Codecasa et al., 2016; Schmidt et al., 2015). The non-intrusive gPC approach used in the current framework is schematically illustrated in Fig. 1.

In this report, we first describe in detail the methodology of the proposed approach. Then we provide and discuss three illustrative examples in order to demonstrate the usefulness and descriptive power of the method in characterizing the fields generated by TMS and tDCS. Finally, we briefly discuss possible generalizations and extensions of the techniques to emphasize its potential as a widely applicable tool for model assessment and optimization.

2. Methods

The calculations of the electric field, in both TMS and tDCS, were conducted with SimNIBS (Thielscher et al., 2015) using a high-resolution finite element model (Fig. 2a). The model consists of tetrahedral elements with an average size of about $1\,mm^3$, resulting in $4.1 \cdot 10^6$ tetrahedra and $7.2 \cdot 10^5$ vertices. The model was used together with the Finite Element Method (FEM) with linear elements to calculate the electric potentials and subsequently the electric fields. Details of the construction of the model and of the FEM calculations can be found in (Nielsen et al., 2018; Windhoff et al., 2013). The investigated setups are shown in Fig. 2c–e. A non-intrusive gPC, implemented in SimNIBS, treats the problem as a black box, that is, it can be applied without any explicit description of the original transfer function that maps the input

parameters $\boldsymbol{\xi}$, (here: tissue conductivities $\boldsymbol{\sigma} = [\sigma_0,...,\sigma_{d-1}]$) (input) to the electric field $\boldsymbol{E}(\boldsymbol{\sigma}, \boldsymbol{r})$ or any other quantity of interest $\boldsymbol{q}(\boldsymbol{\xi})$ (output). This renders the method widely applicable, irrespective of any implementation details of the original problem (Xiu, 2010; Ghanem and Spanos, 1991).

Our initial aim was to describe the uncertainty of the electric field $\boldsymbol{E}(\boldsymbol{\sigma}, \boldsymbol{r})$, where $\boldsymbol{r}$ are the center of the tetrahedra of the mesh representation of gray matter, depending on the uncertainties of the tissue conductivities $\boldsymbol{\sigma}$. That is, we needed to determine the probability density function (PDF) $p(\boldsymbol{E}(\boldsymbol{\sigma}, \boldsymbol{r}))$, considering that the conductivities $\boldsymbol{\sigma}$ are uncertain. The calculation of the PDF involves a large number of function evaluations. However, as field calculations are computationally expensive, a simplified representation of the quantity of interest $\boldsymbol{q}(\boldsymbol{\xi})$, in this case the electric field $\boldsymbol{E}(\boldsymbol{\sigma}, \boldsymbol{r})$, can drastically improve the computational efficiency. A suitable choice to approximate the transfer function is a set of orthogonal polynomials that can span the entire function space. The uncertain tissue conductivities are modeled as mutually independent random variables, described by PDFs with finite variances (e.g., normal, β, or boxcar distributions).

Each PDF $p_i(\sigma_i)$ has to be defined such that it reflects the available measurements of each conductivity parameter σ_i in the best possible way. Here, we used β-distributions in intervals (a_i, b_i), characterized by the shape parameters p_i and q_i:

$$p_i(\sigma_i) = (b_i - a_i)^{1-p_i-q_i} \frac{\Gamma(p_i + q_i)}{\Gamma(p_i)\Gamma(q_i)} (\sigma_i - a_i)^{p_i-1} (b_i - \sigma_i)^{q_i-1} \qquad (1)$$

The parameters assigned to the different tissues are listed in Table 1 and the associated PDFs are shown in Fig. 2b. The distribution type is chosen due to a lack of reliable information about the actual distribution. A bell shaped PDF is expected according to the central limit theorem, and the beta distribution resembles a Gaussian distribution while being bounded at the same time (i.e. negative conductivities are prohibited). The ranges are selected to robustly model the values reported in the available literature. Only experiments were considered, which measured relatively fresh or live tissue (preferably human) at low frequencies (0–100 kHz) near body temperature.

The core concept of the gPC is to find a functional dependence be-
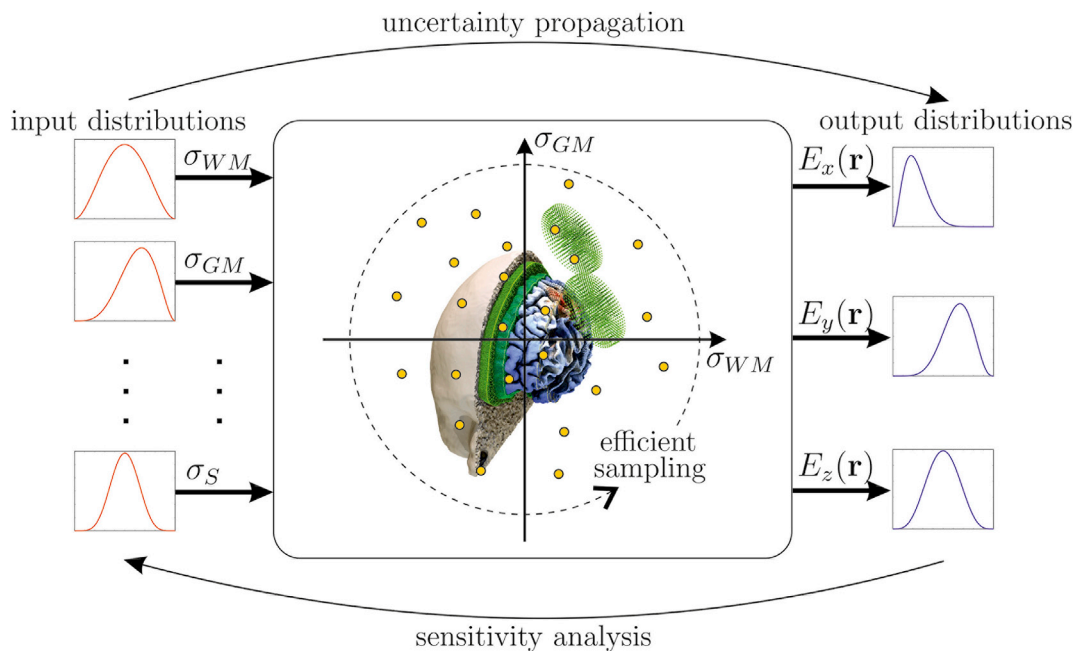

Fig. 1. Principled approach to uncertainty and sensitivity analysis using the non-intrusive generalized polynomial chaos method (gPC). Distributions are defined for the input parameters and efficient sampling of the model allows to expand the solution (here the electric field) with orthogonal polynomial basis functions. The gPC yields the output distributions including the statistical moments as well as their sensitivity with respect to the input parameters.
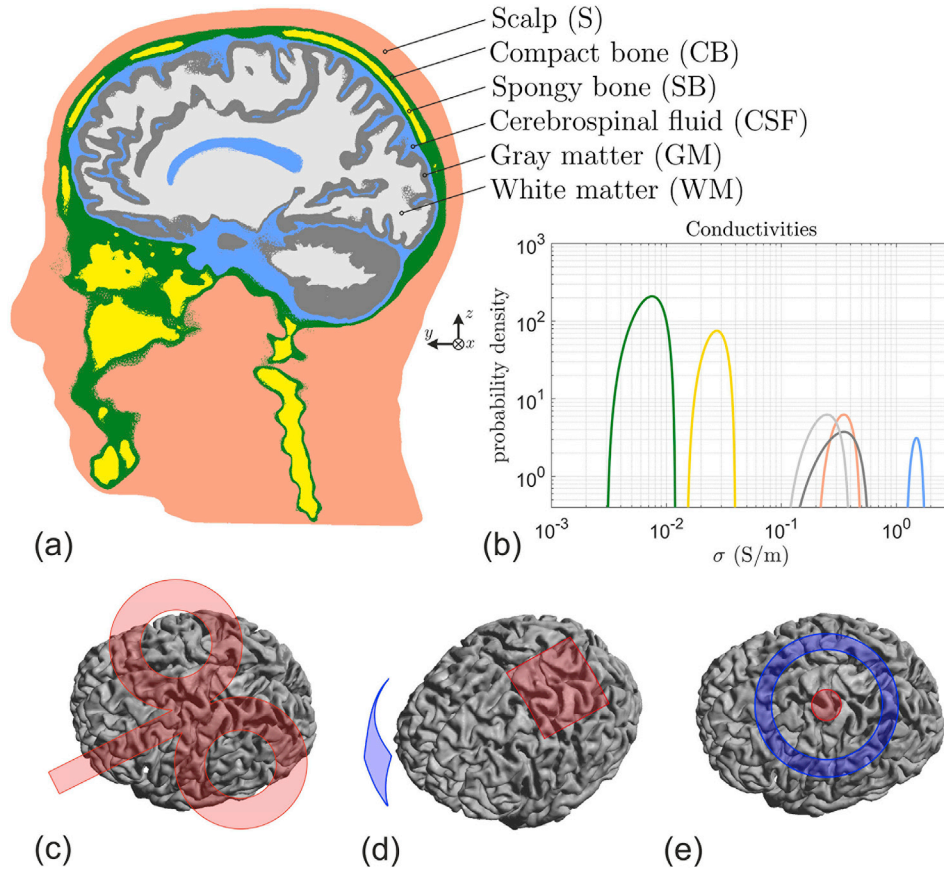
Fig. 2. Simulation setup. (a) Isotropic head model featuring six different tissue types (colors), discretized into $4.1 \cdot 10^6$ tetrahedra and $7.2 \cdot 10^5$ vertices (average size about 1 mm³). (b) Symmetric beta distributions representing the probability density functions of the tissue conductivities, plotted on a double logarithmic scale. The three investigated non-invasive brain stimulation setups (c) TMS, (d) "standard" tDCS, and (e) "focal" tDCS.

Table 1

Limits of the electrical conductivities assigned to the different tissue types. All conductivities are modeled as symmetric bell shaped β-distributions with shape parameters $p = q = 3$. All values in S/m.

Tissue	Min	Max	Reference
White matter (WM)	0.1	0.4	Li et al. (1968)
			Nicholson (1965)
			Akhtari et al. (2010)
Gray matter (GM)	0.1	0.6	Li et al. (1968)
			Ranck (1963)
			Logothetis et al. (2007)
			Yedlin et al. (1974)
Cerebrospinal fluid (CSF)	1.2	1.8	Gabriel et al. (2009)
			Baumann et al. (1997)
Spongy bone (SB)	0.015	0.040	Akhtari et al. (2002)
Compact bone (CB)	0.003	0.012	Akhtari et al. (2002)
			Tang et al. (2008)
Scalp (S)	0.2	0.5	Gabriel et al. (2009)
			Yamamoto and Yamamoto (1976)
			Burger and Milaan (1943)

tween the random variables $\boldsymbol{\xi}$ (such as the conductivities) and the quantity of interest q (such as the electric field at a set of points) by means of an orthogonal polynomial basis Ψ:

$$q(\boldsymbol{\xi}) \approx \sum_{\boldsymbol{\alpha} \in A} \boldsymbol{u}_{\boldsymbol{\alpha}} \Psi_{\boldsymbol{\alpha}}(\boldsymbol{\xi}) \tag{2}$$

The functions $\Psi_{\boldsymbol{\alpha}}(\boldsymbol{\xi}) = \prod_{i=1}^{d} \psi_{\alpha_i}^{i}(\xi_i)$ are the joint polynomial basis functions of the gPC. They are composed of polynomials $\psi_{\alpha_i}^{i}(\xi_i)$ which are separately defined for each random variable. The polynomials are chosen

to be orthogonal in the normed spaced induced by the PDFs $p_i(\sigma_i)$ (Askey and Wilson, 1985). The multi-index $\boldsymbol{\alpha}$ of the joint basis function includes the degrees of the individual polynomials. Along with the construction of the polynomial basis, the gPC coefficients $\boldsymbol{u}_{\boldsymbol{\alpha}}$ that can be used to best approximate the quantity of interest are determined (see section S.2 in the supplementary material for a more detailed description). As a result, an polynomial surrogate of $\boldsymbol{q}(\boldsymbol{\xi})$ as a function of the random input parameters $\boldsymbol{\xi}$ is derived. This enables computationally efficient investigations of their statistics. The applicability of the gPC depends on the type of transfer function to be approximated, that is, the function relating the random variables to the quantity of interest. In its classical form, the gPC is suitable to approximate continuous and smooth transfer functions. This condition is fulfilled here since the gPC is applied to the electric field in every finite element separately, considering continuous changes in the electrical conductivities.

In the current work, the gPC expansion was calculated by drawing samples from the variables $\boldsymbol{\xi}$, in our case the conductivities $\boldsymbol{\sigma}$, according to their probability distributions $p_i(\xi_i)$ and then calculating their corresponding quantity of interest $\boldsymbol{q}(\boldsymbol{\xi})$, such as the electric fields in the positions $\boldsymbol{r}$, $\boldsymbol{E}(\boldsymbol{\sigma}, \boldsymbol{r})$. Starting from a set of basis functions $\Psi_{\boldsymbol{\alpha}}(\boldsymbol{\xi})$, a regression method was used to obtain the gPC coefficients $\boldsymbol{u}_{\boldsymbol{\alpha}}$ based on a set of values for $\boldsymbol{\xi}$ and $\boldsymbol{q}(\boldsymbol{\xi})$. The regression is described in detail in section S.2 of the supplementary material. Afterwards, the error between the gPC approximation and the transfer function $\boldsymbol{q}(\boldsymbol{\xi})$ is estimated using a k-fold cross validation scheme, described in Section S.3 of the supplementary material. If the error remained large, we added more polynomials to the gPC basis $\Psi_{\boldsymbol{\alpha}}(\boldsymbol{\xi})$, drew new samples of the random variables $\boldsymbol{\xi}$ according to their probability distributions, and calculated new values of the quantity of interest $\boldsymbol{q}(\boldsymbol{\xi})$, the regression coefficients $\boldsymbol{u}_{\boldsymbol{\alpha}}$, and updated the error estimate. Based on the data shown in Fig. S3 of the supplementary

material, the number of samples of the random variable $\boldsymbol{\xi}$, and consequently of the quantity of interest per polynomial added to the gPC basis, was set to be twice as high as the number of basis functions ($r = N_s/P = 2$), unless otherwise noted. We called this approach "Adaptive gPC". The algorithm is described in more detail in Section S.3 of the supplementary material and validated in Section S.4. The adaptive nature of the algorithm allows the use of the underlying structure of the problem to quickly determine a reliable set of polynomial basis and coefficients to approximate the transfer function, with minimal human input needed while counteracting overfitting by producing error estimates via cross validation. This is a significant advantage over the classical way to perform gPC, where the investigator has to manually select a set of polynomials for the expansion, as for example in Weise et al. (2015). Unless mentioned otherwise, the adaptive algorithm was run until it reached a relative error of $\varepsilon_0 < 10^{-3}$. This means that the quantities of interest obtained by the gPC approximation, at arbitrary sampling points, are in agreement up to a deviation of about 0.1% with respect to the ones obtained by the original model. This error rate has been chosen to be small so that the errors obtained with the polynomial representation of the transfer function can be neglected for the analysis of the statistical quantities.

Previous studies have compared regression, quadrature, and interpolation based approaches (Ghanem et al., 2016; Weise et al., 2015). It was shown that interpolation and quadrature-based approaches, which use optimal grids with respect to the polynomial families, perform better than regression based gPC, considering the same computational grids. However, this advantage must be balanced against another crucial problem – the correct choice of the approximation order. For non-adaptive approaches with fixed grids, one has to choose the approximation order in advance, which may lead to under- or overfitting and the possibility of using too few or too many sampling points. On the other hand, using adaptive schemes provides an elegant way to overcome this problem and prevent overfitting. Quadrature based adaptive gPC approaches require nested quadrature rules such as Clenshaw-Curtis, which involve an exponential increase in grid size, a method such as Smolyak's to produce sparse grids (Smolyak, 1963), and an expansion rule such as the one proposed in Gerstner and Griebel (2003). The possibility to define different types of probability density functions, and hence different polynomial families, for each random variable requires complex algorithms to extend the grid in every iteration (Agarwal and Aluru, 2011). In contrast, regression based gPC approaches are far more flexible in this concern. They do not require any particularly structured grid to determine the gPC coefficients. For these reasons, we opted for an adaptive gPC algorithm based on regression approaches to iteratively construct the gPC basis.

Once a polynomial surrogate of the quantities of interest is derived using gPC, several statistical quantities can be calculated directly from the coefficients of the polynomial expansion. For example, the expectation (i.e., mean) $\boldsymbol{\mu}$ and variance $\boldsymbol{\nu}$ are determined by:

$$\boldsymbol{\mu} = \boldsymbol{u}_{\boldsymbol{\alpha}_1} \tag{3}$$

$$\boldsymbol{\nu} = \sum_{\boldsymbol{\alpha} \in A \setminus \boldsymbol{\alpha}_1} (\boldsymbol{u}_{\boldsymbol{\alpha}})^2 \tag{4}$$

The relative standard deviation (RSD) with respect to the expectation is then given by RSD $= \sqrt{\boldsymbol{\nu}}/\boldsymbol{\mu}$ and computed position-wise.

For a more complete description of the output PDFs of the electric field, the gPC model has to be sampled using traditional Monte Carlo methods. However, this is possible without much computational effort, because the evaluation of the polynomial description is far less time consuming than the original finite element computation. Typically, it is not a problem to draw 10^6 or more samples. The drawn samples can be fit to appropriate distributions in order to parameterize the PDFs for further evaluations, such as statistical tests.

GPC enables comprehensive analyses to quantify the sensitivity of a

system's output with respect to its input parameters and their uncertainties, and thus to identify the parameters that contribute most to the uncertainty of the output variables. We outline two commonly used measures, namely Sobol indices and global derivative-based sensitivity coefficients. The Sobol indices $S_i^{(v)}$ decompose the total variance $\boldsymbol{\nu}$ of the quantity of interest into components that can be attributed to individual random variables ξ_i or combinations thereof (Sobol, 2001; Sudret 2008). For each $S_i^{(v)}$, we summed the squared coefficients $\boldsymbol{u}_{\boldsymbol{\alpha}}^2$, whose multi-indices $\boldsymbol{\alpha}$ belonged to the set A_i with non-zero values only for the ξ_i of interest.

$$\boldsymbol{S}_i^{(v)} = \frac{1}{\nu} \sum_{\boldsymbol{\alpha} \in A_i} (\boldsymbol{u}_{\boldsymbol{\alpha}})^2 \tag{5}$$

For example, if we want the Sobol coefficient $S_1^{(v)}$, we select $A_1 = \{\{1, 0, \ldots, 0\}, \ldots, \{P, 0, \ldots, 0\}\}$. The Sobol indices were normalized with respect to the total variance $\boldsymbol{\nu}$ and consequently add up to one. In some cases however, it is advantageous to omit this normalization, especially in cases where variances and mean values of different orders of magnitude are investigated at the same time, which is the case for field distributions at, e.g., points with high or almost negligible field intensity. Importantly, Sobol indices reflect the combined effect of the uncertainty of the input parameter and the dependence between the input and output parameters. For example, a low Sobol index could be due to a low uncertainty of the input parameter, a low sensitivity of the output towards the input parameter, or both. As such, Sobol indices are well suited to identify the most important input parameters given our actual (or assumed) knowledge about them.

On the other hand, the global derivative-based sensitivity coefficients $S_i^{(\partial)}$ are measures of the average change of the quantity of interest (here: the electric field) with respect to the i-th random variable. They are determined by means of the gPC-coefficients and the corresponding partial derivatives of the basis functions (Xiu, 2009):

$$\boldsymbol{S}_i^{(\partial)} = \mathbb{E}\left[\frac{\partial \boldsymbol{q}(\boldsymbol{\xi})}{\partial \xi_i}\right] = \sum_{\boldsymbol{\alpha} \in A} \boldsymbol{u}_{\boldsymbol{\alpha}} \int_{\Theta} \frac{\partial \Psi_{\boldsymbol{\alpha}}(\boldsymbol{\xi})}{\partial \xi_i} p(\boldsymbol{\xi}) d\boldsymbol{\xi} \tag{6}$$

In contrast to the Sobol indices, which are stochastic sensitivity measures, derivative-based sensitivity coefficients are deterministic. Analyzing both at the same time may be beneficial since they feature different advantages and disadvantages, as illustrated in Fig. 3. The Sobol index, shown on the left, measures the variance of an output variable due to the variance of an input variable. It is thus sensitive to any sort of relationship between the two variables, which neither needs to be monotonic nor linear and, strictly speaking, not even deterministic (although, in our case, it is). On the other hand, the global derivative reflects the average (linear) sensitivity of an output variable towards an input variable over the range of the input variable. Hence, it is only sensitive to the linear part of the transfer function. A periodic transfer function, for example, would on average show a very low derivative-based sensitivity, whereas the Sobol indices would reveal the actual variation. This being a restriction, derivative-based sensitivities have the advantage that they allow for conclusions on the direction of the influence (proportional or inversely proportional).

Due to the computationally compact representation of the transfer function by gPC, the uncertainty and sensitivity analyses can be efficiently extended to cover a range of complementary quantities of interest. Here, we consider location-wise parameters: (i) the electric field magnitude at each gray matter location and (ii) its normal component relative to the cortical sheet,[1] as well as global parameters: (iii) the 98th percentile of the electric field magnitude as a proxy for stimulation dosage, and (iv) the overall spatial distribution of the field in the gray

---

[1] This component is crucial for the stimulation mechanism, that is, which structures (axons, dendrites) are actually depolarized or hyperpolarized.
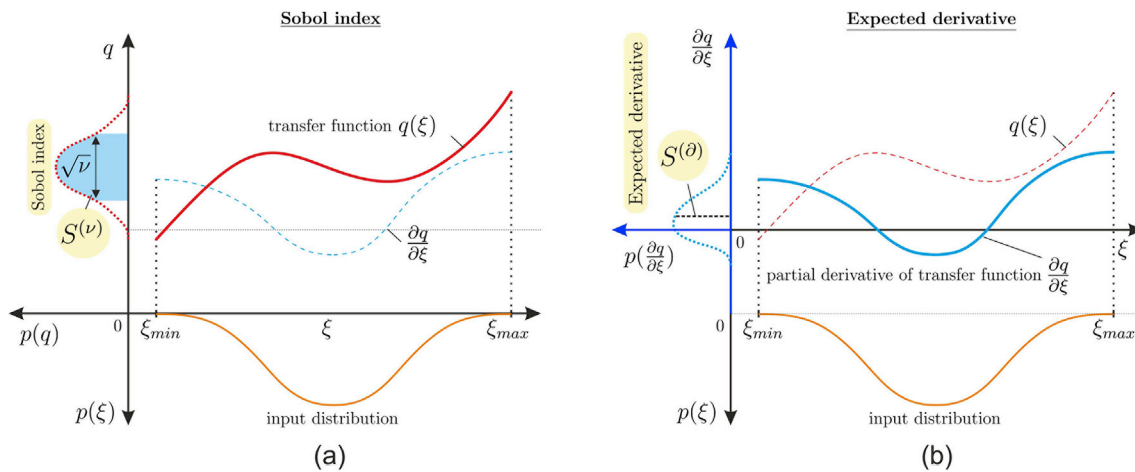
Fig. 3. Graphical representation of (a) the Sobol indices and (b) the expected global derivative based sensitivity coefficients. The Sobol indices quantify the variation of the transfer function (red curve), while the derivative-based sensitivity coefficients provide information about the average derivative over the range of input parameters. Both are weighted with the corresponding probability density functions of the input parameters.

matter.

For the location-wise field magnitudes and the normal components we interpolated the electric field at the $2.9 \cdot 10^5$ vertices of a surface located in the middle layer of gray matter, obtained with FreeSurfer 6.0. The interpolation of the electric fields was performed by first determining the electric field at the nodes of the gray matter volume using the super-convergent patch recovery (Zienkiewicz and Zhu, 1992) and subsequently interpolating the electric field in the nodes of the middle gray matter surface using linear interpolation. For the nodal recovery step, only the electric field values inside gray matter were used. In this way, we improved on the discontinuous gradients of the FEM solutions, and obtained more precise values for the electric field in the region. We determined the electric field magnitude and the normal component of the interpolated electric fields and used the gPC to determine their mean values, the overall uncertainty (variance or relative standard deviation), and their partial uncertainties due to each uncertain tissue conductivity (Sobol indices and global derivatives). For assessing the achievable stimulation strength, we computed the 98th percentile of the field magnitude, which corresponds to the field magnitude that is exceeded in an area of about 40 cm^2. The uncertainty of this value is characterized by computing its distribution and Sobol coefficients.

In order to characterize the impact of the conductivities on the field pattern we used the relative difference measure (RDM) (Meijs et al., 1989) as an index of the difference between the field distribution, for some specific combination of tissue conductivities, and the electric field arising from the mean values of the model parameters:

$$RDM(\bar{x}, \bar{x}_R) = \sqrt{\sum_i \left(\frac{x_i}{\sqrt{\bar{x}^T \cdot \bar{x}}} - \frac{x_{R,i}}{\sqrt{\bar{x}_R^T \cdot \bar{x}_R}} \right)^2} \qquad (7)$$

The vector $\bar{x}$ with the elements x_i ($i = 1 \dots 3N_{tet}$) is the linear concatenation of the electric field vectors in all tetrahedra centers of GM for the parameter combination under investigation, while $\bar{x}_R$ contains the respective values for the reference configuration. In this way, the RDM directly addresses the electric field components and allows the assessment of the impact of conductivity uncertainties on the spatial stimulation patterns, irrespective of the absolute field strengths. We determined the expected variation of the field distribution, arising from the conductivity uncertainties, by calculating the probability density function (pdf) of the RDM. In addition, we identified the conductivities with the strongest influence on the RDM using the Sobol indices.

Three non-invasive brain stimulation setups were investigated as shown in Fig. 2c–e, namely, TMS, standard tDCS and focal tDCS. For TMS, the coil position was above the left motor cortex. A typical figure-8

coil (Magstim 70 mm) was centered above the hand knob of the precentral gyrus, with the coil handle pointing to the anterior direction. A normalized rate of change of the coil current of $dI/dt = 1$ A/μs was used. Please note that our conclusions do not depend on this choice, and that the results can be easily rescaled to give the field strengths at, e.g. average motor threshold (Thielscher and Kammer, 2002).

For standard tDCS, a motor cortex montage was used with one electrode pad above the left hand knob (5×5 cm^2; 4 mm gel and 4 mm rubber layers, with conductivities 1 S/m and 0.1 S/m) and a second electrode pad over the right supraorbital region (5×7 cm^2; 4 mm gel and 4 mm rubber layers, with conductivities 1 S/m and 0.1 S/m). For each of the electrodes, the upper surface was set to a fixed potential corresponding to the Dirichlet boundary conditions, and the results were later scaled to ensure a current of 1 mA. For the "focal" tDCS setup, a motor cortex montage was used with a central round electrode pad (2 cm diameter; 4 mm gel and 4 mm rubber layers, with conductivities 1 S/m and 0.1 S/m) and a surrounding ring electrode (7.5 cm and 10 cm inner and outer diameters; 4 mm gel and 4 mm rubber layers, with conductivities 1 S/m and 0.1 S/m).

3. Results

3.1. Overview

We will start with a general overview of the results before presenting the findings for each of the three examples in more detail. The gPC converged after 58 (TMS), 292 (focal tDCS), and 176 (standard tDCS) FEM simulations. The gPC matrices [Ψ] in the last step of the adaptive algorithm were of size $[N \times P] = [58 \times 29]$ (TMS), $[292 \times 146]$ (focal tDCS), and $[176 \times 88]$ (standard tDCS) and thus invertible with moderate computational cost in a short time. The maximum polynomial orders of the basis obtained with the adaptive algorithm are shown in Table 2.

We interpolated the electric fields obtained during the expansion of $E(\sigma, r)$ in a middle layer of gray matter, calculated the field strength and normal component and expanded these quantities using the same set of polynomials as used for the original expansion. The cross-validation errors of the resulting expansions were $< 1.5 \cdot 10^{-3}$ for all modalities and both quantities of interest.

The remaining calculation steps only involved matrix-matrix multiplications with the coefficient matrices [U] and the solution matrices [E]. The coefficient matrices [U] were of size $[29 \times 287666]$ (TMS), $[146 \times 287666]$ (focal tDCS), and $[88 \times 287666]$ (standard tDCS), and the solution matrices [E] were of size $[58 \times 287666]$ (TMS), $[292 \times 287666]$ (focal tDCS), and $[176 \times 287666]$ (standard tDCS). Fig. 4

Table 2

Maximum polynomial orders and interaction orders of the polynomial basis obtained for the gPC expansion of the electric field with the adaptive algorithm. The maximum polynomial order was defined as the maximum order of any individual polynomial $\psi_{\alpha_i}^i$, and the maximum interaction order is the maximum number of different variables involved in a polynomial basis Ψ^α. For example, if we have the set of multi-indices $A = \{\alpha_1 = \{0, 0, 0\}, \alpha_2 = \{1, 0, 0\}, \alpha_3 = \{0, 1, 0\}, \alpha_4 = \{1, 1, 0\}, \alpha_5 = \{2, 0, 0\}, \alpha_6 = \{3, 0, 0\}\}$, the maximum polynomial order will be 3, due to the term α_6, where the first polynomial is of degree 3, and its maximum interaction order 2, due to the term α_4, where the first and second random variable interact.

Simulation	Maximum Polynomial Order	Maximum Interaction Order
TMS	5	2
Focal tDCS	8	4
Standard tDCS	6	3

illustrates electric field strength in a given position (chosen to be the one with the mean electric field strength closest to the 99th percentile), as a function of gray and white matter conductivities. In the first column, we see the values obtained from sampling the FEM model, and in the second column, values obtained from sampling the gPC model. We can see that both yield very similar results, and divergences tend to happen mostly in low probability regions, as shown in the difference plots (right column). The expected (mean) field strengths in middle cortical sheet are shown in Fig. 5a, and their uncertainty is characterized by the relative standard deviation (RSD) and overall variance (VAR; Fig. 5a and top row of 5b). The individual contributions of the conductivity uncertainties to the overall variance are represented by the Sobol indices (Fig. 5b). In addition, they are characterized by the global-derivative-based sensitivity coefficients in Fig. 6. Both measures convey similar information. Whereas the Sobol indices are intuitively interpretable as portions of the overall variance, the sensitivity coefficients have the advantage that they convey directional information.

The 98th percentiles were also calculated using the field interpolated at the middle layer of gray matter. For this quantity, using the same set of polynomials as for the expansion of $\boldsymbol{E}(\boldsymbol{\sigma}, \boldsymbol{r})$, we obtained cross validation results $< 1.6 \cdot 10^{-3}$. Fig. 7 shows how the electric field strength, that is exceeded on a cortical area of about 40 cm^2, is affected by the conductivity uncertainties. It can be seen that the relative standard deviation for TMS is much smaller than that of tDCS, meaning that uncertainties in the tissue conductivity values affect the TMS electric fields less than the tDCS electric fields.

The effects of stimulation are not only dependent on the field strength, but also on the field direction. Therefore, Fig. 8 depicts the
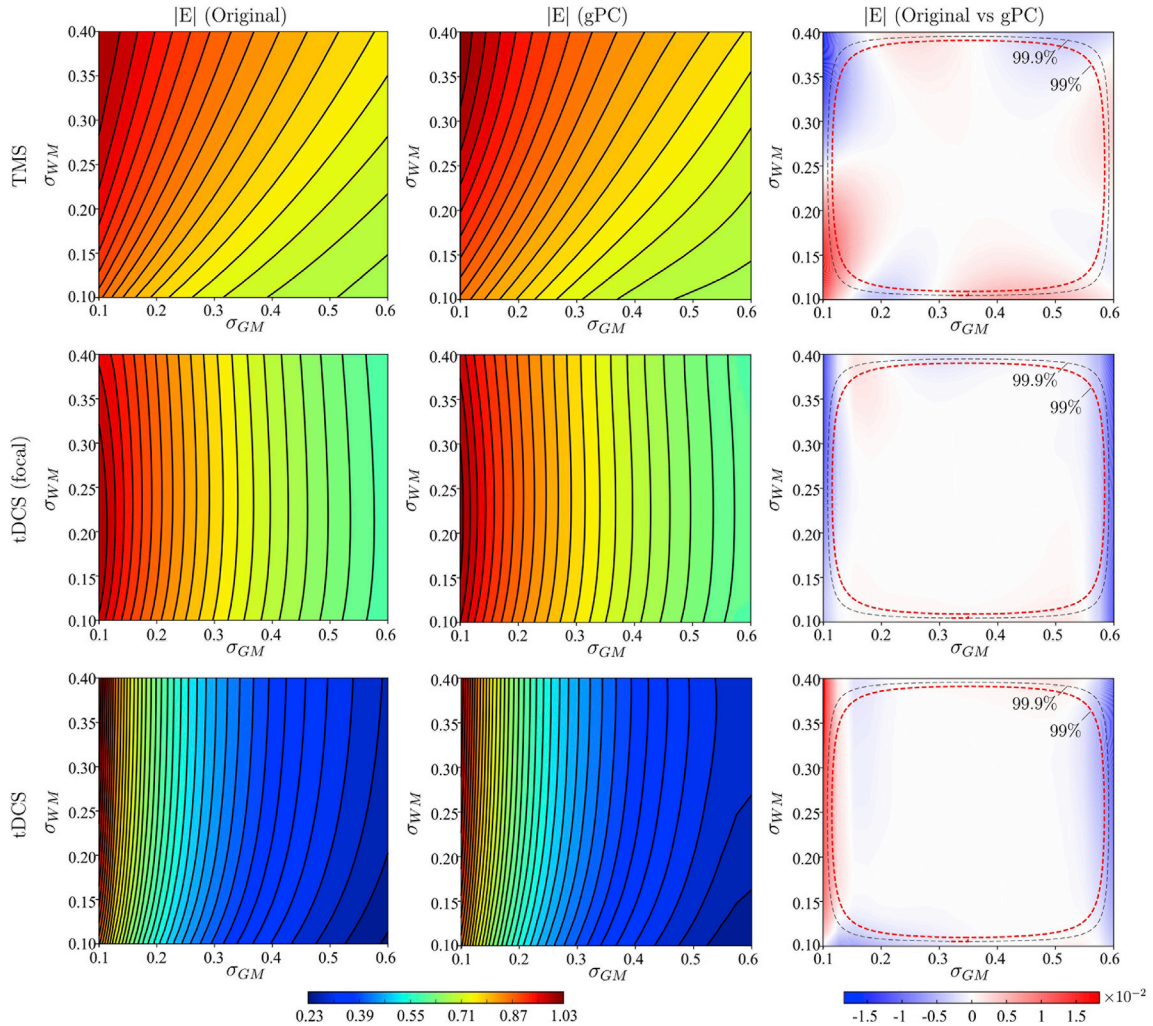

Fig. 4. Comparison of the electric field magnitude $|\boldsymbol{E}|$ (in V/m) in a given position, as a function of gray and white matter conductivities, σ_{GM} and σ_{WM}, obtained either from sampling the original FEM model (left column) or from sampling the gPC approximation (central column) for TMS (top row), focal tDCS (middle row), and standard tDCS (bottom row). Both models were sampled in a uniform grid of 20×20 GM and WM conductivity points, while the other conductivities were kept constant at their mean values. The difference between the original model function and the gPC approximation is shown on the right. The electric fields shown correspond to the positions where the mean electric field strength is closest to the 99th percentile.
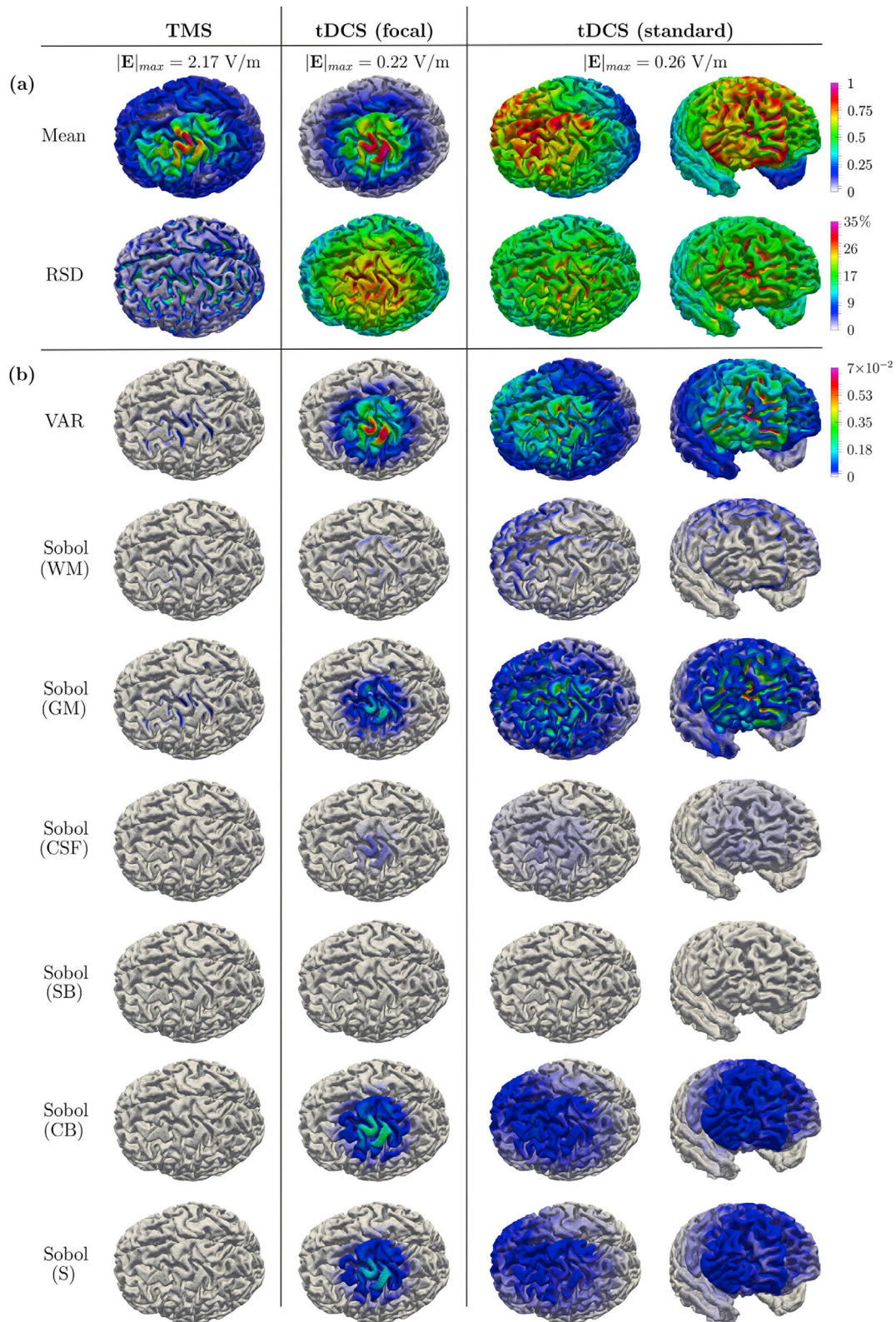
Fig. 5. Simulation results of the electric field magnitude |**E**| on the middle GM surface. (a) Mean and relative standard deviation (RSD) of the electric field strength. In order to compare the different stimulation methods, the mean distributions were normalized to their respective maximum values and the RSD distributions were determined with respect to the corresponding mean values at each location. (b) Total variance (VAR) and Sobol indices $S_i^{(\nu)}$ associated with each tissue type (for tissue abbreviations see Fig. 1a). VAR and Sobol indices were normalized with respect to the individual squared maxima of the mean distributions of the stimulation modalities to provide comparability.

ARTICLE IN PRESS

G.B. Saturnino et al.   NeuroImage xxx (xxxx) xxx
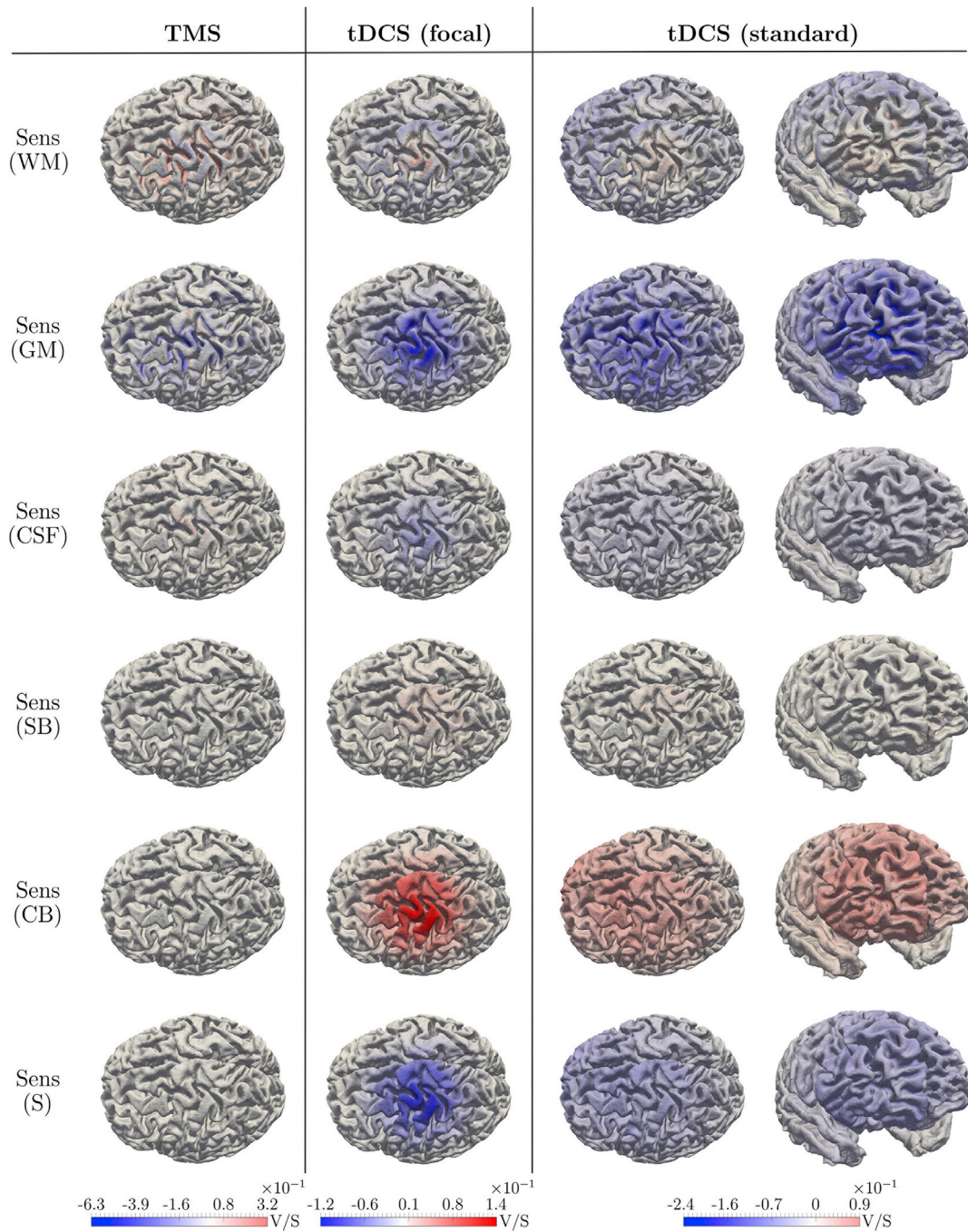
Fig. 6. Global derivative based sensitivity coefficients $S_i^{(\partial)}$ of the electric field magnitude $|E|$ on the middle GM surface associated with each tissue type (for tissue abbreviations see Fig. 1a). Blue reflects negative relation between tissue conductivity and field strength, and red a positive relation. White reflects little to no correlation.

results of the gPC analysis for the normal component of the electric field, showing similar dependencies as in case of the magnitude of the electric field.

Finally, the influence of conductivity variations on the overall field pattern was quantified by means of a gPC analysis with the RDM as the quantity of interest. However, by performing the gPC using the same set of simulations and polynomials as for $E(\sigma, r)$, as done in the previous cases, we obtained large cross-validation errors in the order of $4 \cdot 10^{-1}$. To obtain a reliable RDM gPC approximation, we applied the adaptive algorithm limiting the number of simulations to 1000. The ratio of samples per polynomial was increased from 2 to 5, and the coefficients were calculated using Tikhonov regularized regression. After these

modifications, the errors decreased to $4.5 \cdot 10^{-2}$ for TMS, $5.7 \cdot 10^{-2}$ for the focal tDCS, and $5.7 \cdot 10^{-2}$ for standard tDCS. The polynomial orders for the RDM expansions are shown in Table 3. During the analysis, the conductivities of GM and WM were identified as the most important model parameters. Because the gPC of the RDM was more intricate than for the electric field, we also re-evaluated the model fit by systematically sampling across σ_{GM} and σ_{WM}, while keeping the other conductivities at their mean values. This is illustrated in Fig. 9, showing that a low RDM occurs as long as the ratio between GM and WM conductivities is within a certain (quite broad) range. It can be observed that the gPC is more accurate in the center of the parameter space, where the joint probability density is highest. As in Fig. 4, the most significant errors happen in the
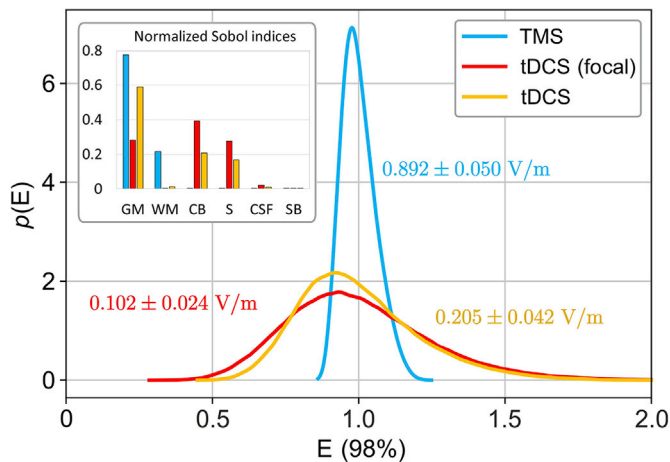
Fig. 7. Probability density functions of the 98th percentile of the electric field strength for the three stimulation methods. This corresponds to a cortical area of 40 cm^2 (total area 2000 cm^2). The distributions are normalized with respect to their individual mean in order to provide comparability. The absolute values of the mean and the corresponding standard deviation are also provided and color coded accordingly.

corner regions. Conductivity values in this region are highly unlikely, as indicated by the 99th and 99.9th percentile boundaries, highlighted by dashed lines in the figure.

The PDFs of the RDM are shown in Fig. 10. In order to convey a visual impression of the severity of the expected field pattern changes, as revealed by the pdfs, exemplary field patterns for an RDM of 0.2 are shown. In addition, the normalized Sobol indices are depicted in Fig. 11 to provide more detailed insight into the composition of the variance of the RDM.

3.2. TMS

For TMS, the mean of the electric field (Fig. 5a) shows a focal distribution on the gyral crowns. RSD and VAR (Fig. 5a and b) reveal a much higher uncertainty in the sulcal walls (20–25%) than on the gyral crowns ($<$5%). The Sobol indices (Fig. 5b) show that the uncertainties of GM and WM conductivities are the main sources of the uncertainty of the electric field strength, explaining approximately 75% and 23% of VAR, respectively. The remaining tissues play a minor role.

The results of the global-derivative-based sensitivity (Fig. 6) confirm these findings and additionally reveal the directionality of the effects. For example, an increased conductivity of WM results in an increase of the electric field in GM, which indicates a direct proportionality (positive derivative, red color). In contrast, an increase in GM conductivity reduces the field magnitude, which indicates an inverse relationship (negative derivative, blue color). These effects can be explained by the law of current conservation and Ohm's law. Increasing GM conductivity decreases the electric potential drop and therefore the electric field strength in GM. Interestingly, increasing the conductivity of neighboring WM increases the electric field in GM. Considering Ohm's law, it is expected that an increase in conductivity will increase the current density in the respective domain. In the presence of boundaries however, the law of current conservation has to be fulfilled, i.e. the normal component of the current density has to be continuous, which leads to an increase of the electric field in neighboring domains.

For the 98th percentile of the field magnitude, the standard deviation is only about 5.6% of the mean, and the Sobol indices reveal, in accordance to the location-wise results above, that almost all of the variance is due to GM and WM conductivity uncertainties.

The results for the normal component of the electric field (Fig. 8) show that misestimating the conductivities can result in deviations in the sulcal walls where the normal component is high. The main contributors

to the deviations were again GM and WM conductivity uncertainties.

The probability density function of the RDM shown in Fig. 10 indicates that the influence of the conductivities on the pattern of the electric field was small. More specifically, it is very unlikely that the RDM would exceed a value of 0.25. Additionally, the normal and tangential components of the electric field are shown in order to get a visual impression on how the electric field patterns differ between the reference solution considering the mean conductivities and a conductivity combination resulting in an RDM of 0.2. Both field maps are normalized to their respective maxima, since the RDM quantifies differences in field shape and not in magnitude. Contrary to expectations, the actual field pattern was only weakly influenced by conductivity variations, even when considering a worst case scenario of conductivity combinations resulting in an RDM of 0.2. The similarity between both field solutions shows that the conductivities only weakly influence the actual spatial pattern of the field, in contrast to the field magnitude generated in the cortex as observed in Fig. 5.

Inspecting the Sobol indices (Fig. 11) reveals that only the GM and WM conductivities notably influence the RDM. Interestingly, a substantial part of the variance is explained by the interaction between these two.

3.3. Focal tDCS

The mean distribution of the electric field for focal tDCS resembles the one of TMS (Fig. 5), but the uncertainty is generally higher. The RSD for the field magnitude was high in the sulcal fundi (~33%) and on the gyral crowns (~27%). The variance showed a similar pattern. The Sobol indices revealed that the main contributors to the variance were the uncertainties of the conductivities of compact bone (~40%), GM (~30%), and scalp (~25%), minor contributions came from WM (~3%) and CSF (~2%). Similar results were obtained for the global-derivative-based sensitivities shown in Fig. 6, which underline that the conductivities of compact bone, GM and scalp have the strongest influence on the field strength. Expectedly, increases in compact bone conductivity led to increases of the electric field in GM, as more current passes through bone in that case. In contrast, an increase in scalp conductivity tends to "short circuit" or "shunt" the current along the head surface and in consequence decreases the electric field. These effects were mainly present at the gyral crowns below the central electrode.

The standard deviation of the 98th percentile of the magnitude was about 23.5% of the mean, which is much larger than the uncertainty found for TMS. The Sobol indices confirmed the findings for the location-wise results (significant contributions by GM, compact bone and skin).

The results for the normal component of the electric field are shown in Fig. 8. In contrast to TMS, it can be observed that the normal component was primarily uncertain on the gyral crowns, where for this modality the normal component is highest. The main contributors were again the conductivities of GM, compact bone, and skin.

Fig. 8 reveals a similar dependency of RDM upon the gray and white matter conductivities as for TMS.

The probability density function of the RDM shows only slightly larger values compared to TMS (Fig. 10). Correspondingly, no strong difference in field shape can be observed when comparing normal and tangential components of the electric field between the reference and RDM = 0.2. The normalized Sobol indices in Fig. 11 show that the field pattern was again mainly influenced by the GM and WM conductivities and their interaction, but also that other tissues such as cortical bone (CB) have moderate influence.

3.4. Standard tDCS

As expected, standard tDCS results in a far more widespread field distribution than focal tDCS (Fig. 5a). Near the frontal electrode, the field peaked in the sulcal fundi, whereas the highest values occurred on the gyral crowns for the brain regions close to the central electrode. RSD and
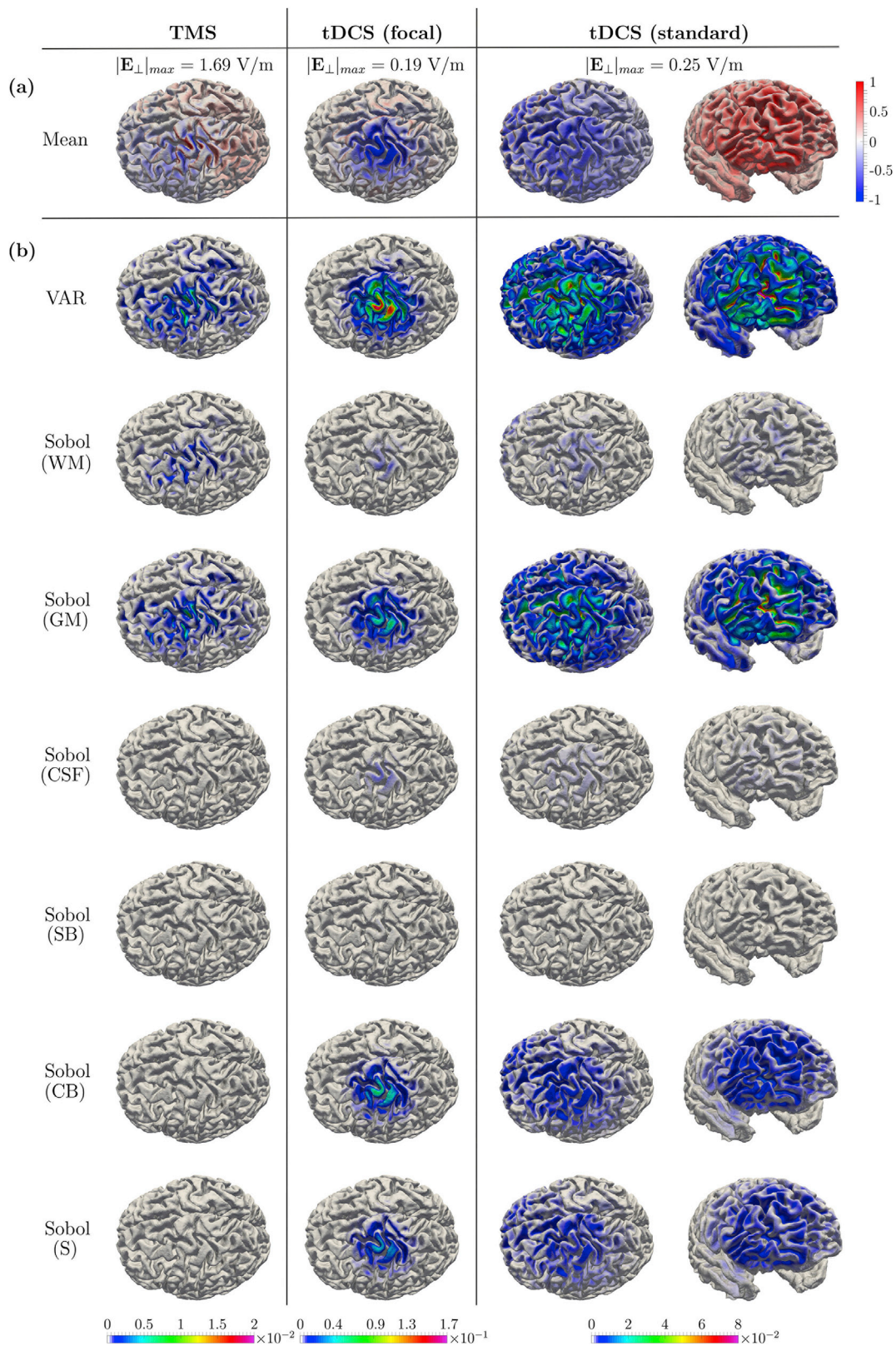
Fig. 8. Simulation results of the normal component of the electric field on the middle GM surface. Inflowing electric fields have negative values and are shown in blue. (a) Mean (b) Total variance (top row) and Sobol indices $S_i^{(v)}$ associated with each tissue type (for tissue abbreviations see Fig. 1a). VAR and Sobol indices were normalized with respect to the individual squared maxima of the mean distributions of the stimulation modalities to provide comparability.

Table 3

Maximum polynomial orders and interaction orders of the polynomial basis obtained with the adaptive algorithm for the RDM expansion. For an explanation of the items in the table, please refer to Table 2.

Simulation	Maximum Polynomial Order	Maximum Interaction Order
TMS	18	3
Focal tDCS	11	3
Standard tDCS	20	4

VAR were consistently high in the sulcal fundi near the electrodes (up to 30%), with the Sobol indices identifying the conductivity uncertainties of GM (~77%), compact bone (~10%), and scalp (~7%) as the main contributors. These findings were confirmed by the derivative-based sensitivity coefficients (Fig. 6).

The standard deviation of the 98th percentile was about 20.5% of the mean, thus similar to focal tDCS and much larger than for TMS. Again, the Sobol indices reflect the findings for the location-wise field magnitudes.

Considering the normal component of the electric field in Fig. 8, it can be observed that conductivity uncertainties primarily influenced the latter in the sulcal fundi and adjacent walls. Similar to focal tDCS, the main contributors were the conductivities of GM, compact bone, and skin.

The RDM pattern (Fig. 9) and the probability density function of the RDM (Fig. 10) were very similar to that of focal tDCS. The shape of the electric field differed slightly between the reference and RDM = 0.2,

which can be explained by the more widespread field distribution in the case of standard tDCS compared to focal tDCS and TMS. The Sobol indices presented in Fig. 11 are very similar to focal tDCS, except for a slightly lower influence of the conductivities of compact bone and skin.

4. Discussion and conclusion

We used a pipeline based on non-intrusive gPC in order to comprehensively characterize the impact of uncertain tissue conductivities on the magnitude, direction, and overall pattern of the electric field for three exemplary non-invasive brain stimulation setups. The uncertainty range of field strengths obtained for tDCS (Fig. 7) agrees well with the results presented in Opitz et al. (2016), Huang et al. (2017), and Huang et al. (2018) obtained by direct invasive measurements of the fields generated by 1 mA tDCS in patients.

We demonstrated that our approach yields detailed insight into the spatially dependent impact of conductivity parameter uncertainties on uncertainties of the electric field caused by TMS and tDCS. We found that for all investigated scenarios the magnitude of the electric field is most affected (Figs. 5–7), while the field direction and the global field topography are less sensitive to the conductivity uncertainties (Figs. 9–11). In other words, accurate knowledge of the individual conductivities is much more important for quantitative dosage control than for targeting (Peterchev et al., 2012). Consequently, interindividual conductivity differences could potentially contribute to the widely observed interindividual threshold differences observed in non-invasive brain stimulation (mainly TMS) experiments. We also found that
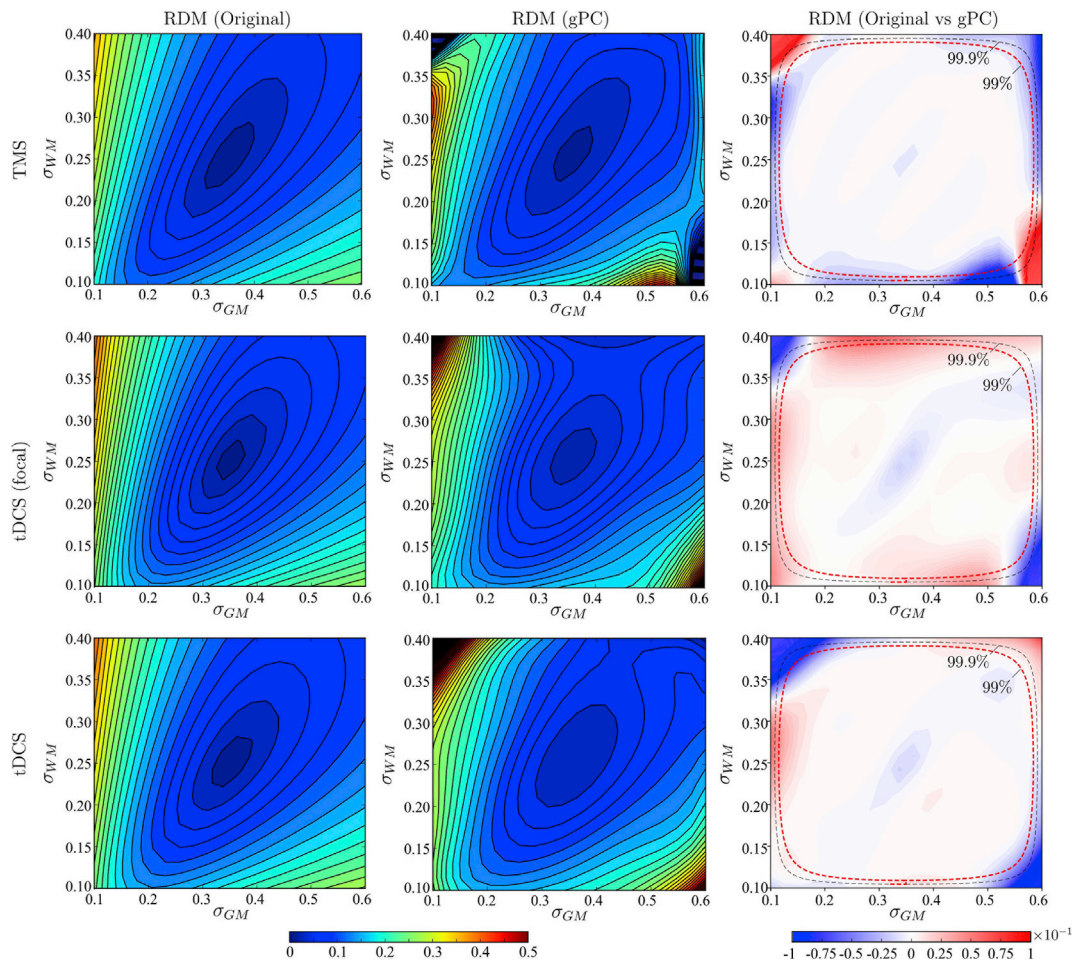

Fig. 9. RDM as a function of the two most significant conductivities σ_{GM} and σ_{WM} for TMS (top row), tDCS focal (middle row), and tDCS (bottom row). In this particular analysis, the original model function (left column) and the gPC approximation (central column) were sampled on a uniform grid of 20×20 conductivity points. The difference between the original model function and the gPC approximation is shown on the right.
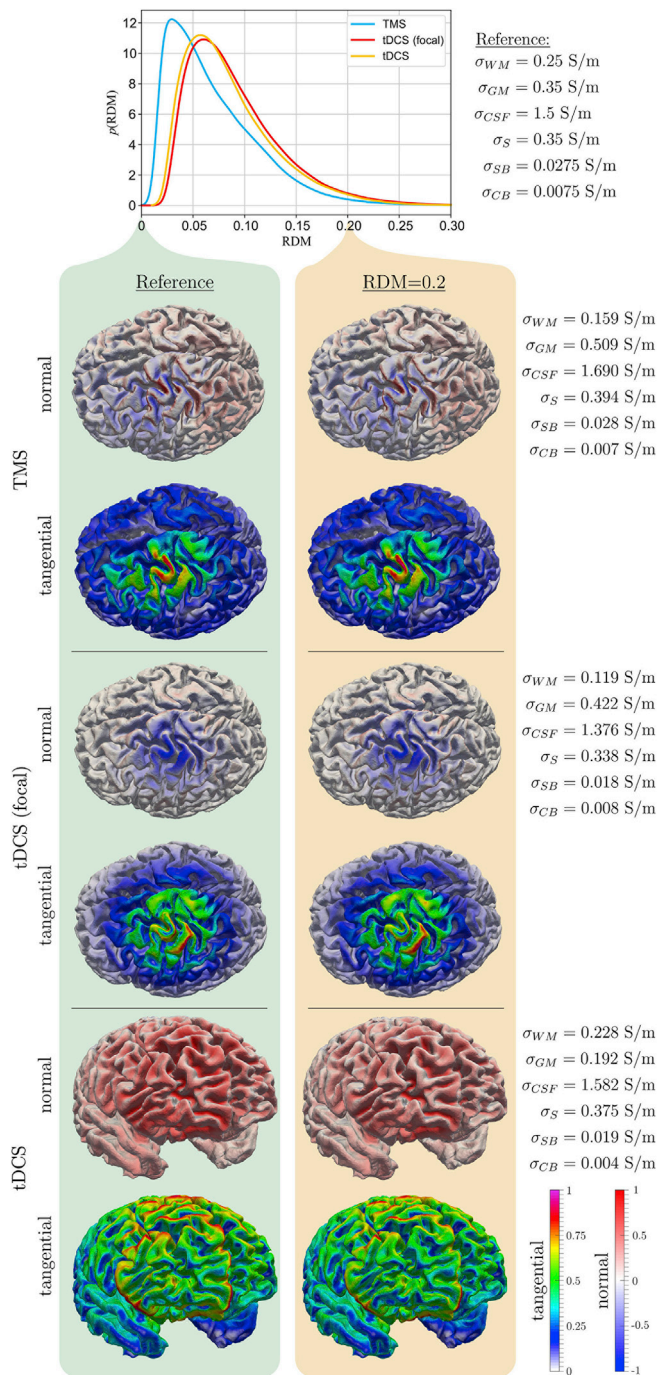
Fig. 10. Probability density functions of the RDM for TMS, focal tDCS and standard tDCS. The normal and tangential components of the electric field are shown for the reference electric field calculated with the average values of all conductivities, and the conductivities that correspond to an RDM of 0.2. It is emphasized that the distributions were normalized to their respective maximum values to focus on the variability in field shape and not in field magnitude (cf. Fig. 3).

TMS-induced fields are less affected by conductivity variations than those caused by tDCS. TMS is primarily influenced by uncertainties of the gray and white matter conductivities, whereas tDCS also depends on the conductivities of compact bone and scalp.

In addition, we identified specific differences between the modalities with respect to the most severely affected locations on the cortex. For example, the magnitude of the electric field caused by TMS can be predicted accurately on the gyral crowns (at the field maximum) but is less accurate in the sulcal walls, whereas focal tDCS is less accurate on the gyral crowns and in the sulcal fundi. For standard tDCS, the main inaccuracy occurs in the sulcal fundi.

The present work focuses on conductivity variations and not on anatomical inaccuracies of the modeled head volume conductor. It can be assumed that the latter also strongly contributes to uncertainties in the field estimates. Specifically, the results presented here point towards a low influence of the uncertainty of CSF conductivity on the field estimates. On the other hand, Nielsen et al. (2018) (Fig. 6b), have shown clear differences in the cortical electric fields for two head models that differ in the level of detail used for modeling the CSF-filled sulci. Taking these two findings together, it can be stated that varying CSF conductivity within the range reported in the literature alters the field in GM only weakly, while replacing part of CSF by GM in the model clearly changes the field pattern.

The employed non-intrusive gPC allows for a "black box" approach to the system under investigation. This ensures maximal generalizability because a closed analytical description of the problem is not needed. The gPC can be easily post-processed to determine statistical moments or sensitivities. Moreover, large numbers of parameter combinations can be evaluated quickly, in a Monte Carlo sense, due to the parsimonious polynomial description of the transfer function to determine the output PDFs. In contrast, direct Monte Carlo sampling (Toschi et al., 2012) or parameter grid sampling (Salvador et al., 2012) of the original transfer function would require $> 10^5$ FEM simulations for this number of input parameters (6 parameters) to reach the desired accuracy. Other approaches that seek to reduce the computational effort, such as worst case evaluation (Thielscher et al., 2011) or linearization (Santos et al., 2016), are much more limited in their conclusions. Gomez et al. investigated the impact of varying conductivities, brain size and coil positions on the induced electric field in TMS using a collocation-based high-dimensional model representation approach (CUT-HDMR) (Gomez et al., 2015; Rabitz et al, 1999). Their analysis was restricted to the mean and the STD of the electric field, omitting a detailed sensitivity analysis and any other higher order quantities such as the RDM or the 98th percentile of the electric field. In contrast to ours and other studies (Weise et al., 2015; Codecasa et al., 2016), Gomez et al. (2015) reported that conductivity variations have a negligible effect on TMS operation compared to uncertainties in coil position or brain size. However, they assumed very large and uniformly distributed angle deviations, in a range between 0° and 90°, which potentially obscures the effect of conductivity variation, since their iterative approach expands the model in terms of the variables with the highest influence. In our study, the electrical conductivities were modelled assuming bell shaped beta distributions, which are more biologically plausible than uniform distributions. An advantage of our approach, compared to interpolation methods, is that it assures orthogonality between the basis functions in the normed spaced induced by the PDFs. Consequently, the statistical moments and the sensitivities can be calculated directly from the gPC coefficients. The moderately sized gPC matrix has to be inverted only once to determine all of the coefficients for all of the investigated points inside the brain. In summary, the proposed approach is advantageous in terms of (i) adaptivity, i.e. it assists the investigator when analyzing "black-box" systems by adding polynomials to the basis, which are improving the approximation quality. By avoiding unused polynomials, the number of forward calculations needed to derive the gPC approximation is reduced significantly; (ii) fast convergence rate (see Supplemental Material Section S.4); (iii) a stable and efficient error estimator using a k-fold cross validation without the need for additional model evaluations (see Supplemental Material Section S.4); and (iv) the use of a regression approach allows to reduce constraints on the set of sampling points when setting up the gPC basis adaptively. This allows for extra flexibility for expanding polynomials and defining input PDFs.

The proposed formulation allows the direct extraction of uncertainties of, for example, the electric field and sensitivities towards specific input parameters. These properties enable systematic
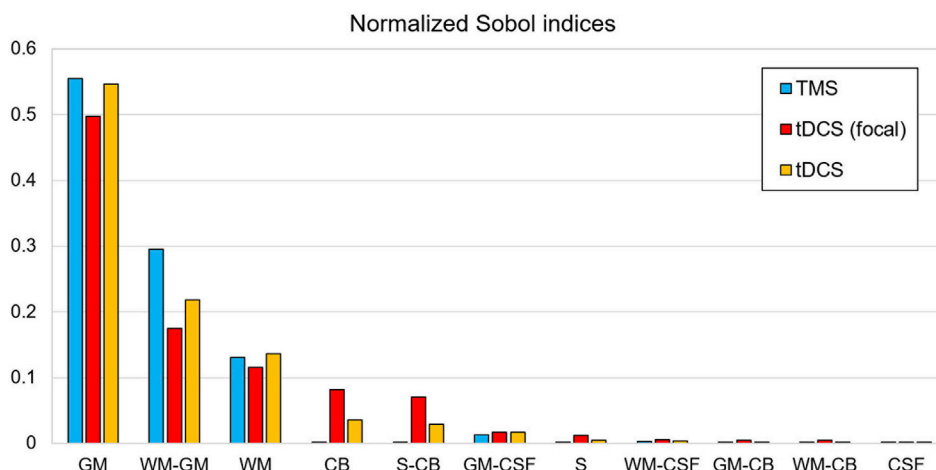
Fig. 11. Most significant normalized Sobol indices of the RDM for TMS, tDCS and tDCS (focal) itemizing the composition of the variance of the RDM (cf. the probability density functions from Fig. 7).

investigations of systems with computationally expensive transfer functions (such as the FEM calculation in our case) and large parameter sets. An important advantage of gPC is that the expansion can be performed with respect to quantities of interest other than the electric field itself, allowing for uncertainty analyses also for higher-level parameters such as the RDM. With the information provided by this and similar analyses, the relevance of accurate knowledge of tissue conductivities for particular stimulation situations can be quantified and research aiming at targeted measurements of distinct tissue types can be directed.

The gPC yields a highly efficient meta-model of the complex transfer function that can also be used in a variety of further applications. One further example is optimization studies. Conductivity optimizations, as they were conducted by Huang et al. (Huang et al., 2017; Huang et al., 2018), could be solved in a very elegant and time-efficient manner. We could also use the polynomial surrogates to quickly perform MC-based uncertainty quantification analyses in quantities of interest where gPC does not work well, such as the RDM.

Besides the classical FEM, there are other approaches to calculating electric fields from TMS and tDCS sources, such as discontinuous Galerkin FEM (DG-FEM) (Engwer et al., 2017), which have the property of being current preserving and are therefore more accurate, especially in regions close to tissue boundaries and where the skull becomes excessively thin, causing current to leak through the skull compartment. However, as we are interested in the middle of the tissue, and as when creating the head model we imposed a condition that tissue boundaries should not overlap. we believe that the increase in accuracy from DG-FEM methods and other advanced solvers for elliptical PDEs would probably not change the results of the current uncertainty quantification analysis. In fact, Engwer et al. noticed in the context of EEG forward simulations that the difference in accuracy between traditional FEM and DG-FEM is not large when the model is of sufficiently high resolution (bellow 2 mm), as our model is. However, with such methods the post-processing steps might be easier to implement, as the electric field resulting from the calculations is not piecewise-constant.

In conclusion, the presented methodology constitutes a very flexible and efficient tool to assess the reliability of the predictions of brain stimulation models and to identify the crucial model parameters. This depends on the particular stimulation configuration and region(s) of interest. Even though the present demonstration is limited to an initial set of three scenarios, tested on a single head model, our current study reveals important differences between the simulated stimulation methods that likely generalize across individuals. Furthermore, the method offers great potential for the characterization of other models as well as other applications, such as model inversion, for example in EEG/MEG source reconstruction.

Appendix A. Supplementary data

Supplementary data to this article can be found online at https://doi.org/10.1016/j.neuroimage.2018.12.053.

References

Agarwal, N., Aluru, N.R., 2011. Weighted Smolyak algorithm for solution of stochastic differential equations on non-uniform probability measures. Int. J. Numer. Methods Eng. 85 (11), 1365–1389.

Akhtari, M., Bryant, H.C., Mamelak, A.N., Flynn, E.R., Heller, L., Shih, J.J., Mandelkern, M., Matlachov, A., Ranken, D.M., Best, E.D., DiMauro, M.A., Lee, R.R., Sutherling, W.W., 2002. Conductivities of three-layer live human skull. Brain Topogr. 14 (3), 151–167. https://doi.org/10.1023/A:1014590923185.

Akhtari, M., Mandelkern, M., Bui, D., Salamon, N., Vinters, H.V., Mathern, G.W., 2010. Variable anisotropic brain electrical conductivities in epileptogenic foci. Brain Topogr. 23 (3), 292–300. https://doi.org/10.1007/s10548-010-0144-z.

Askey, R., Wilson, J.W., 1985. Some basic hypergeometric orthogonal polynomials that generalize Jacobi-polynomials. Memoir. Am. Math. Soc. 54 (319), 1–55, 9780821860557.

Baumann, S.B., Wozny, D.R., Kelly, S.K., Meno, F.M., 1997. The electrical conductivity of human cerebrospinal fluid at body temperature. IEEE Trans. Biomed. Eng. 44 (3), 220–223. https://doi.org/10.1109/10.554770.

Burger, H.C., Milaan, J.B., 1943. Measurements of the specific resistance of the human body to direct current. Acta Med. Scand. 114, 584–607. https://doi.org/10.1111/j.0954-6820.1943.tb11253x.

Codecasa, L., Di Rienzo, L., Weise, K., Gross, S., Haueisen, J., 2016. Fast MOR-based approach to uncertainty quantification in transcranial magnetic stimulation. IEEE Trans. Magn. 52 (3), 7200904. https://doi.org/10.1109/TMAG.2015.2475120.

Engwer, C., Vorwerk, J., Ludewig, J., Wolters, C.H., 2017. A discontinuous Galerkin method to solve the EEG forward problem using the subtraction approach. SIAM J. Sci. Comput. 39 (1), B138–B164. https://doi.org/10.1137/15M1048392.

Gabriel, C., Gabriel, S., Corthout, E., 1996. The dielectric properties of biological tissues: I. Literature survey. Phys. Med. Biol. 41 (11), 2231–2249 (PMID: 8938024).

Gabriel, C., Peyman, A., Grant, E.H., 2009. Electrical conductivity of tissue at frequencies below 1 MHz. Phys. Med. Biol. 54 (16), 4863–4878. https://doi.org/10.1088/0031-9155/54/16/002.

Geddes, L.A., Baker, L.E., 1967. The specific resistance of biological material - a compendium of data for the biomedical engineer and physiologist. Med. Biol. Eng. Comput. 5 (3), 271–293. https://doi.org/10.1007/BF02474537.

Gerstner, T., Griebel, M., 2003. Dimension–adaptive tensor–product quadrature. Computing 71 (1), 65–87. https://doi.org/10.1007/s00607-003-0015-5.

Ghanem, R., Higdon, D., Owhadi, H., 2016. Handbook of Uncertainty Quantification. Springer, Cham. https://doi.org/10.1007/978-3-319-12385-1.

Ghanem, R.G., Spanos, P., 1991. Stochastic Finite Elements: a Spectral Approach. Springer, New York, ISBN 978-1-4612-3094-6.

Gomez, L., Yucel, A., Hernandez-Garcia, L., Taylor, S., Michielssen, E., 2015. Uncertainty quantification in transcranial magnetic stimulation via high dimensional model

representation. IEEE Trans. Biomed. Eng. 61 (1), 361–372. https://doi.org/10.1109/TBME.2014.2353993.

Huang, Y., Liu, A.A., Lafon, B., Friedman, D., Dayan, M., Wang, X., Bikson, M., Doyle, W.K., Devinsky, O., 2017. Parra LC Measurements and models of electric fields in the in vivo human brain during transcranial electric stimulation. eLife 6, e18834. https://doi.org/10.7554/eLife.18834.

Huang, Y., Liu, A.A., Lafon, B., Friedman, D., Dayan, M., Wang, X., Bikson, M., Doyle, W.K., Devinsky, O., 2018. Parra LC Correction: measurements and models of electric fields in the in vivo human brain during transcranial electric stimulation. eLife 6, e35178. https://doi.org/10.7554/eLife.35178.

Li, C., Bak, A.F., Parker, L.O., 1968. Specific resistivity of the cerebral cortex and white matter. Exp. Neurol. 20 (4), 544–557. https://doi.org/10.1016/0014-4886(68)90108-8.

Logothetis, N.K., Kayser, C., Oeltermann, A., 2007. In vivo measurement of cortical impedance spectrum in monkeys: implications for signal propagation. Neuron 55 (5), 809–823. https://doi.org/10.1016/j.neuron.2007.07.027.

Meijs, J.W.H., Weier, O.W., Peters, M.J., van Oosterom, A., 1989. On the numerical accuracy of the boundary element method (EEG application). IEEE Trans. Biomed. Eng. 36 (10), 1038–1049. https://doi.org/10.1109/10.40805.

Nicholson, P.W., 1965. Specific impedance of cerebral white matter. Exp. Neurol. 13 (4), 386–401. https://doi.org/10.1016/0014-4886(65)90126-3.

Nielsen, J.D., Madsen, K.H., Puonti, O., Siebner, H.R., Bauer, C., Madsen, C.G., Saturnino, G.B., Thielscher, A., 2018. Automatic skull segmentation from MR images for realistic volume conductor models of the head: assessment of the state-of-the-art. Neuroimage 174 (1), 587–598. https://doi.org/10.1016/j.neuroimage.2018.03.001.

Opitz, A., Paulus, W., Will, S., Antunes, A., Thielscher, A., 2015. Determinants of the electric field during transcranial direct current stimulation. Neuroimage 109, 140–150. https://doi.org/10.1016/j.neuroimage.2015.01.033.

Opitz, A., Falchier, A., Yan, C.G., Yeagle, E.M., Linn, G.S., Megevand, P., Thielscher, A., Deborah, A.R., Milham, M.P., Mehta, A.D., Schroeder, C.E., 2016. Spatiotemporal structure of intracranial electric fields induced by transcranial electric stimulation in humans and nonhuman primates. Sci. Rep. 6, 31236. https://doi.org/10.1038/srep31236.

Peterchev, A.V., Wagner, T.A., Miranda, P.C., Nitsche, M.A., Paulus, W., Lisanby, S.H., Pascual-Leone, A., Bikson, M., 2012. Fundamentals of transcranial electric and magnetic stimulation dose: definition, selection, and reporting practices. Brain Stimul 5 (4), 435–453. https://doi.org/10.1016/j.brs.2011.10.001.

Rabitz, H., Aliş, Ö.F., Shorter, J., Shim, K., 1999. Efficient input—output model representations. Comput. Phys. Commun. 117 (1–2), 11–20.

Ranck, J.B., 1963. Specific impedance of rabbit cerebral cortex. Exp. Neurol. 7, 144–152. https://doi.org/10.1016/S0014-4886(63)80005-9.

Salvador, R., Ramirez, F., V'yacheslavovna, M., Miranda, P.C., 2012. Effects of tissue dielectric properties on the electric field induced in tDCS: a sensitivity analysis. Conf. Proc. IEEE Eng. Med. Biol. Soc. 787–790. https://doi.org/10.1109/EMBC.2012.6346049.

Santos, L., Martinho, M., Salvador, R., Wenger, C., Fernandes, S.R., Ripolles, O., Ruffini, G., Miranda, P.C., 2016. Evaluation of the electric field in the brain during transcranial direct current stimulation: a sensitivity analysis. 2016. In: 38th Annual International Conference of the IEEE Engineering in Medicine and Biology Society. EMBC), Orlando, FL, pp. 1778–1781. https://doi.org/10.1109/EMBC.2016.7591062.

Schmidt, C., Wagner, S., Burger, M., van Rienen, U., Wolters, C.H., 2015. Impact of uncertain head tissue conductivity in the optimization of transcranial direct current stimulation for an auditory target. J. Neural. Eng. 12 (4), 46028. https://doi.org/10.1088/1741-2560/12/4/046028.

Smolyak, S., 1963. Quadrature and interpolation formulas for tensor products of certain classes of functions. Dokl. Akad. Nauk SSSR 4 (5), 240–243.

Sobol, I.M., 2001. Global sensitivity indices for nonlinear mathematical models and their Monte Carlo estimates. Math. Comput. Simulat. 55 (1–3), 271–280. https://doi.org/10.1016/S0378-4754(00)00270-6.

Sudret, B., 2008. Global sensitivity analysis using polynomial chaos expansions. Reliab. Eng. Syst. Saf. 93 (7), 964–979. https://doi.org/10.1016/j.ress.2007.04.002.

Tang, C., You, F., Cheng, G., Gao, D., Fu, F., Yang, G., Dong, X., 2008. Correlation between structure and resistivity variations of the live human skull. IEEE Trans. Biomed. Eng. 55 (9), 2286–2292. https://doi.org/10.1109/TBME.2008.923919.

Toschi, N., Keck, M.E., Welt, T., Guerrisi, M., 2012. Quantifying uncertainty in Transcranial Magnetic Stimulation - a high resolution simulation study in ICBM space. Conf. Proc. IEEE Eng. Med. Biol. Soc. 1218–1221. https://doi.org/10.1109/EMBC.2012.6346156.

Thielscher, A., Kammer, T., 2002. Linking physics with physiology in TMS: a sphere field model to determine the cortical stimulation site in TMS. Neuroimage 17 (3), 1117–1130. https://doi.org/10.1006/nimg.2002.1282.

Thielscher, A., Opitz, A., Windhoff, M., 2011. Impact of the gyral geometry on the electric field induced by transcranial magnetic stimulation. Neuroimage 54 (1), 234–243. https://doi.org/10.1016/j.neuroimage.2010.07.061.

Thielscher, A., Antunes, A., Saturnino, G.B., 2015. Field modeling for transcranial magnetic stimulation: a useful tool to understand the physiological effects of TMS? Ann. Int. Conf. IEEE Eng. Med. Biol. Soc. 222–225. https://doi.org/10.1109/EMBC.2015.7318340.

Weise, K., Di Rienzo, L., Brauer, H., Haueisen, J., Toepfer, H., 2015. Uncertainty analysis in transcranial magnetic stimulation using non-intrusive polynomial chaos expansion. IEEE Trans. Magn. 51 (7), 5000408. https://doi.org/10.1109/TMAG.2015.2390593.

Wiener, N., 1938. The homogeneous chaos. Am. J. Math. 60 (4), 897–936. https://doi.org/10.2307/2371268.

Windhoff, M., Opitz, A., Thielscher, A., 2013. Electric field calculations in brain stimulation based on finite elements: an optimized processing pipeline for the generation and usage of accurate individual head models. Hum. Brain Mapp. 34 (4), 923–935. https://doi.org/10.1002/hbm.21479.

Xiu, D., 2009. Fast numerical methods for stochastic computations: a review. Commun. Comput. Phys. 5 (2–4), 242–272.

Xiu, D., 2010. Numerical Methods for Stochastic Computations. A Spectral Method Approach. Princeton University Press, Princeton, ISBN 9780691142128.

Yamamoto, T., Yamamoto, Y., 1976. Electrical properties of the epidermal stratum corneum. J. Med. Biol. Eng. 14 (2), 151–158. https://doi.org/10.1007/BF02478741.

Yedlin, M., Kwan, H., Murphy, J.T., Nguyen-Huu, H., Wong, Y.C., 1974. Electrical conductivity in cat cerebellar cortex. Exp. Neurol. 43 (3), 555–569. https://doi.org/10.1016/0014-4886(74)90195-2.

Zienkiewicz, O.C., Zhu, J.Z., 1992 May 30. The superconvergent patch recovery and a posteriori error estimates. Part 1: the recovery technique. Int. J. Numer. Methods Eng. 33 (7), 1331–1364. https://doi.org/10.1002/nme.1620330702.